

Clouds in the atmosphere of the super-Earth exoplanet GJ 1214b

Laura Kreidberg¹, Jacob L. Bean¹, Jean-Michel Désert^{2,3}, Björn Benneke⁴, Drake Deming⁵, Kevin B. Stevenson¹, Sara Seager⁴, Zachory Berta-Thompson⁶, Andreas Seifahrt¹, & Derek Homeier⁷

¹*Department of Astronomy and Astrophysics, University of Chicago, Chicago, IL 60637*

²*CASA, Department of Astrophysical & Planetary Sciences, University of Colorado, Boulder, CO 80309*

³*Department of Astronomy, California Institute of Technology, Pasadena, CA 91101*

⁴*Department of Physics, Massachusetts Institute of Technology, Cambridge, MA 02139*

⁵*Department of Astronomy, University of Maryland, College Park, MD 20742*

⁶*Department of Astronomy, Harvard University, Cambridge, MA 02138*

⁷*Centre de Recherche Astrophysique de Lyon, ENS Lyon, Lyon, France*

Recent surveys have revealed that planets intermediate in size between Earth and Neptune (“super-Earths”) are among the most common planets in the Galaxy¹⁻³. Despite their ubiquity, these planets have unknown nature and origin because there are no super-Earths in our Solar System, and because the available data for the extrasolar examples are insufficient to fully characterize them^{4,5}. Atmospheric studies are a natural next step toward developing a comprehensive understanding of this new class of object. Substantial previous work has focused on using transmission spectroscopy to characterize the atmosphere of the exoplanet GJ 1214b because it is the most easily observed transiting super-Earth⁶⁻²³. However, these previous measurements did not have sufficient precision to determine the composition of the planet’s atmosphere. The atmosphere of GJ 1214b could be dominated by heavy elements, such as water (e.g., a 100% water vapor composition), or the atmosphere could have high-altitude clouds that obscure its lower layers. Here we present a precise measurement of the transmission spectrum of GJ 1214b in the near infrared based on an intensive observational campaign with the Hubble Space Telescope. These data are inconsistent (at greater than 5σ confidence) with cloud-free models for the planet’s atmosphere with water-, methane-, carbon monoxide-, or carbon dioxide-dominated compositions. The planet’s atmosphere must contain clouds to be consistent with the observed featureless spectrum.

We observed 13 transits of the planet GJ 1214b with the Wide Field Camera 3 (WFC3) instrument on the Hubble Space Telescope (HST) between UT 27 September 2012 and 4 August 2013. Each transit observation consisted of four orbits of the telescope, with 45-minute gaps in phase coverage between target visibility periods due to Earth occultation. We obtained time-series spectroscopy from 1.1 to 1.7 μm during each observation. The data were taken in spatial scan mode, which slews the telescope during the exposure and moves the spectrum perpendicular to the dispersion direction on the detector. This mode reduces the instrumental overhead time by a factor of five over staring mode observations. We achieved an integration efficiency of 60 – 70%. We extracted the spectra and divided each exposure into five-pixel-wide bins, obtaining spectro-

photometric time series in 22 channels (resolution $R \equiv \lambda/\Delta\lambda \sim 70$). The typical signal-to-noise per 88.4 s exposure per channel was 1,400. We also created a “white” light curve summed over the entire wavelength range. Our analysis incorporates data from 11 of the 13 transits observed, because one observation was compromised due to a telescope guiding error and another showed evidence of a starspot crossing.

The light curves exhibit ramp-like systematics comparable to those seen in previous WFC3 data^{12,24,25}. The ramp in the first orbit of each visit consistently has the largest amplitude. Following standard procedure for HST transit light curves, we did not include data from the first orbit in our analysis, leaving 597 exposures. We corrected for systematics in the remaining three orbits using two techniques which have been successfully applied in prior analyses^{12,24,26}. The first approach models the systematics as an analytic function of time. The function includes an exponential ramp term fit to each orbit, a visit-long slope, and a normalization factor. The second approach assumes the morphology of the systematics is independent of wavelength, and models each channel with a scalar multiple of the time-series of systematics from the white light curve fit. We obtained consistent results from both methods, and report here results from the second. See the Supplementary Information for more detail on the observations, data reduction, and systematics correction.

We fit the light curves in each spectroscopic channel with a transit model²⁷ to measure the transit depth as a function of wavelength; this constitutes the transmission spectrum. See Figure 1 for the fitted transit light curves. We used the second systematics correction technique described above and fit a unique planet-to-star radius ratio R_p/R_s and normalization C to each channel and each visit, and a unique linear limb darkening parameter u to each channel. We assumed a circular orbit and fixed the inclination $i = 89.1^\circ$, the ratio of the semi-major axis to the stellar radius $a/R_s = 15.25$, the orbital period $P = 1.58040464894$ days, and the time of central transit $T_c = 2454966.52507$ BJD_{TDB}. These are the best fit values to the white light curve. The measured transit depths in each channel are consistent over all transit epochs, and we report the weighted average depth per channel. The resulting transmission spectrum is shown in Figure 2.

GJ 1214b must have an atmosphere, because interior structure models for the planet require a nonzero mass fraction of volatiles to explain the observed planetary mass and radius⁵. Transmission spectroscopy has the potential to probe the atmospheric composition of GJ 1214b. The technique is primarily sensitive to the mean molecular weight of the atmosphere and the abundance and opacity of the absorbing species. Previous measurements of the transmission spectrum lacked the precision required to determine the nature of the planet’s atmosphere. Both a high mean molecular weight composition and a hydrogen-rich atmosphere with high-altitude clouds were consistent with the observations.

The transmission spectrum we report here has the precision necessary to detect spectral features for a high mean molecular weight atmosphere. However, the observed spectrum is feature-

less. The data are best fit with a flat line, which has a reduced χ^2 of 1.1. We compare several models to the data that represent limiting case scenarios in the range of expected atmospheric compositions²⁸. Depending on the formation history and evolution of the planet, a high mean molecular weight atmosphere could be dominated by water (H₂O), methane (CH₄), carbon monoxide (CO), carbon dioxide (CO₂), or spectrally inactive nitrogen (N₂). Water is expected to be the dominant absorber in the wavelength range of our observations, so a wide range of high mean molecular weight atmospheres with trace amounts of water can be approximated by a pure H₂O model. The data show no evidence for water absorption. A cloud-free pure H₂O composition is ruled out at 15.7 σ confidence. In the case of a dry atmosphere, features from other absorbers such as CH₄, CO, or CO₂ could dominate the transmission spectrum. Cloud-free atmospheres composed of these absorbers are also excluded by the data, at 29.4, 7.2, and 5.4 σ confidence, respectively. A CO₂ atmosphere is the most challenging to detect because CO₂ has the highest mean molecular weight and a relatively small opacity in the observed wavelength range. Given that the data are precise enough to rule out even a CO₂ composition at high confidence, the most likely explanation for the absence of spectral features is a gray opacity source, suggesting that clouds are present in the atmosphere. Clouds can block transmission of stellar flux through the atmosphere, which truncates spectral features arising from below the cloud altitude.

To illustrate the properties of potential clouds, we perform a Bayesian analysis on the transmission spectrum with a code designed for spectral retrieval of super-Earth atmospheric compositions²⁹. We assume a two-component model atmosphere of water and a solar mix of hydrogen/helium gas, motivated by the fact that water is the most abundant icy volatile for solar abundance ratios. Clouds are modeled as a gray opacity source below a given altitude. See Figure 3 for the retrieval results. For this model, the data constrain the cloud top pressure to less than 10⁻² mbar for a mixing ratio with mean molecular weight equal to solar and less than 10⁻¹ mbar for a water-dominated composition (both at 3 σ confidence). At the temperatures and pressures expected in the atmosphere of GJ 1214b, equilibrium condensates of ZnS and KCl can form in the observable part of the atmosphere. While these species could provide the necessary opacity, they are predicted to form at much higher pressures (deeper than 10 mbar for a 50x solar metallicity model)²¹, requiring that clouds be lofted high from their base altitude to explain our measured spectrum. Alternatively, photochemistry could produce a layer of hydrocarbons at low pressures in the upper atmosphere, analogous to the haze on Saturn’s moon Titan^{19,21}.

The result presented here demonstrates the capability of current facilities to measure very precise spectra of exoplanets by combining many transit observations. This observational strategy has the potential to yield the atmospheric characterization of an Earth-like planet orbiting a small, nearby star. Such a planet could have spectral features comparable in size to the photon-limited measurement precision we obtained with the Hubble Space Telescope. However, our findings for the super-Earth archetype GJ 1214b, as well as emerging results for hot, giant exoplanets^{24,30}, suggest that clouds may be pervasive across a wide range of planetary atmosphere compositions, temperatures, and pressures. Making further progress in this area will require obtaining high-precision

data over a wider wavelength range than is currently possible. Fortunately, the next generation of large ground-based telescopes and the James Webb Space Telescope will have the capabilities to make these kinds of measurements, bringing us within reach of characterizing potentially habitable worlds beyond our Solar System.

1. Cassan, A. *et al.* One or more bound planets per Milky Way star from microlensing observations. *Nature* **481**, 167–169 (2012).
2. Fressin, F. *et al.* The False Positive Rate of Kepler and the Occurrence of Planets. *Astrophys. J.* **766**, 81 (2013).
3. Petigura, E. A., Marcy, G. W. & Howard, A. W. A Plateau in the Planet Population below Twice the Size of Earth. *Astrophys. J.* **770**, 69 (2013).
4. Adams, E. R., Seager, S. & Elkins-Tanton, L. Ocean Planet or Thick Atmosphere: On the Mass-Radius Relationship for Solid Exoplanets with Massive Atmospheres. *Astrophys. J.* **673**, 1160–1164 (2008).
5. Rogers, L. A. & Seager, S. Three Possible Origins for the Gas Layer on GJ 1214b. *Astrophys. J.* **716**, 1208–1216 (2010).
6. Bean, J. L., Miller-Ricci Kempton, E. & Homeier, D. A ground-based transmission spectrum of the super-Earth exoplanet GJ 1214b. *Nature* **468**, 669–672 (2010).
7. Désert, J.-M. *et al.* Observational Evidence for a Metal-rich Atmosphere on the Super-Earth GJ1214b. *Astrophys. J.* **731**, L40 (2011).
8. Croll, B. *et al.* Broadband Transmission Spectroscopy of the Super-Earth GJ 1214b Suggests a Low Mean Molecular Weight Atmosphere. *Astrophys. J.* **736**, 78 (2011).
9. Crossfield, I. J. M., Barman, T. & Hansen, B. M. S. High-resolution, Differential, Near-infrared Transmission Spectroscopy of GJ 1214b. *Astrophys. J.* **736**, 132 (2011).
10. Bean, J. L. *et al.* The Optical and Near-infrared Transmission Spectrum of the Super-Earth GJ 1214b: Further Evidence for a Metal-rich Atmosphere. *Astrophys. J.* **743**, 92 (2011).
11. de Mooij, E. J. W. *et al.* Optical to near-infrared transit observations of super-Earth GJ 1214b: water-world or mini-Neptune? *Astron. Astrophys.* **538**, A46 (2012).
12. Berta, Z. K. *et al.* The Flat Transmission Spectrum of the Super-Earth GJ1214b from Wide Field Camera 3 on the Hubble Space Telescope. *Astrophys. J.* **747**, 35 (2012).
13. Murgas, F. *et al.* Narrow band H α photometry of the super-Earth GJ 1214b with GTC/OSIRIS tunable filters. *Astron. Astrophys.* **544**, A41 (2012).
14. Fraine, J. D. *et al.* Spitzer Transits of the Super-Earth GJ1214b and Implications for its Atmosphere. *Astrophys. J.* **765**, 127 (2013).

15. Narita, N. *et al.* Multi-color Transit Photometry of GJ 1214b through BJHK_s Bands and a Long-term Monitoring of the Stellar Variability of GJ 1214. *Astrophys. J.* **773**, 144 (2013).
16. Teske, J. K., Turner, J. D., Mueller, M. & Griffith, C. A. Optical observations of the transiting exoplanet GJ 1214b. *Mon. Not. R. Astron. Soc.* **431**, 1669–1677 (2013).
17. de Mooij, E. J. W. *et al.* Search for Rayleigh Scattering in the Atmosphere of GJ1214b. *Astrophys. J.* **771**, 109 (2013).
18. Narita, N. *et al.* IRSF SIRIUS JHK_s Simultaneous Transit Photometry of GJ 1214b. *Proc. Astron. Soc. Japan* **65**, 27 (2013).
19. Miller-Ricci Kempton, E., Zahnle, K. & Fortney, J. J. The Atmospheric Chemistry of GJ 1214b: Photochemistry and Clouds. *Astrophys. J.* **745**, 3 (2012).
20. Howe, A. R. & Burrows, A. S. Theoretical Transit Spectra for GJ 1214b and Other ”Super-Earths”. *Astrophys. J.* **756**, 176 (2012).
21. Morley, C. V. *et al.* Quantitatively Assessing the Role of Clouds in the Transmission Spectrum of GJ 1214b. *ArXiv e-prints* (2013). 1305.4124.
22. Benneke, B. & Seager, S. How to Distinguish between Cloudy Mini-Neptunes and Water/Volatile-Dominated Super-Earths. *ArXiv e-prints* (2013). 1306.6325.
23. Barstow, J. K., Aigrain, S., Irwin, P. G. J., Fletcher, L. N. & Lee, J.-M. Constraining the atmosphere of GJ 1214b using an optimal estimation technique. *ArXiv e-prints* (2013). 1306.6567.
24. Deming, D. *et al.* Infrared Transmission Spectroscopy of the Exoplanets HD 209458b and XO-1b Using the Wide Field Camera-3 on the Hubble Space Telescope. *Astrophys. J.* **774**, 95 (2013).
25. Swain, M. *et al.* Probing the extreme planetary atmosphere of WASP-12b. *Icarus* **225**, 432–445 (2013).
26. Stevenson, K. B. *et al.* Transmission Spectroscopy of the Hot-Jupiter WASP-12b from 0.7 to 5 microns. *ArXiv e-prints* (2013). 1305.1670.
27. Mandel, K. & Agol, E. Analytic Light Curves for Planetary Transit Searches. *Astrophys. J.* **580**, L171–L175 (2002).
28. Fortney, J. J. *et al.* A Framework for Characterizing the Atmospheres of Low-Mass Low-Density Transiting Planets. *ArXiv e-prints* (2013). 1306.4329.
29. Benneke, B. & Seager, S. Atmospheric Retrieval for Super-Earths: Uniquely Constraining the Atmospheric Composition with Transmission Spectroscopy. *Astrophys. J.* **753**, 100 (2012).

30. Pont, F., Knutson, H., Gilliland, R. L., Moutou, C. & Charbonneau, D. Detection of atmospheric haze on an extrasolar planet: the 0.55-1.05 μm transmission spectrum of HD 189733b with the HubbleSpaceTelescope. *Mon. Not. R. Astron. Soc.* **385**, 109–118 (2008).

Supplementary Information is available in the online version of the paper.

Acknowledgements This work is based on observations made with the NASA/ESA Hubble Space Telescope that were obtained at the Space Telescope Science Institute, which is operated by the Association of Universities for Research in Astronomy, Inc., under NASA contract NAS 5-26555. These observations are associated with program GO-13021. Support for this work was provided by NASA through a grant from the Space Telescope Science Institute, the National Science Foundation through a Graduate Research Fellowship (to L.K.), the Alfred P. Sloan Foundation through a Sloan Research Fellowship (to J.L.B.), NASA through a Sagan Fellowship (to J.-M.D.), and the European Research Council (for D.H. through an ERC Advanced Grant to Gilles Chabrier).

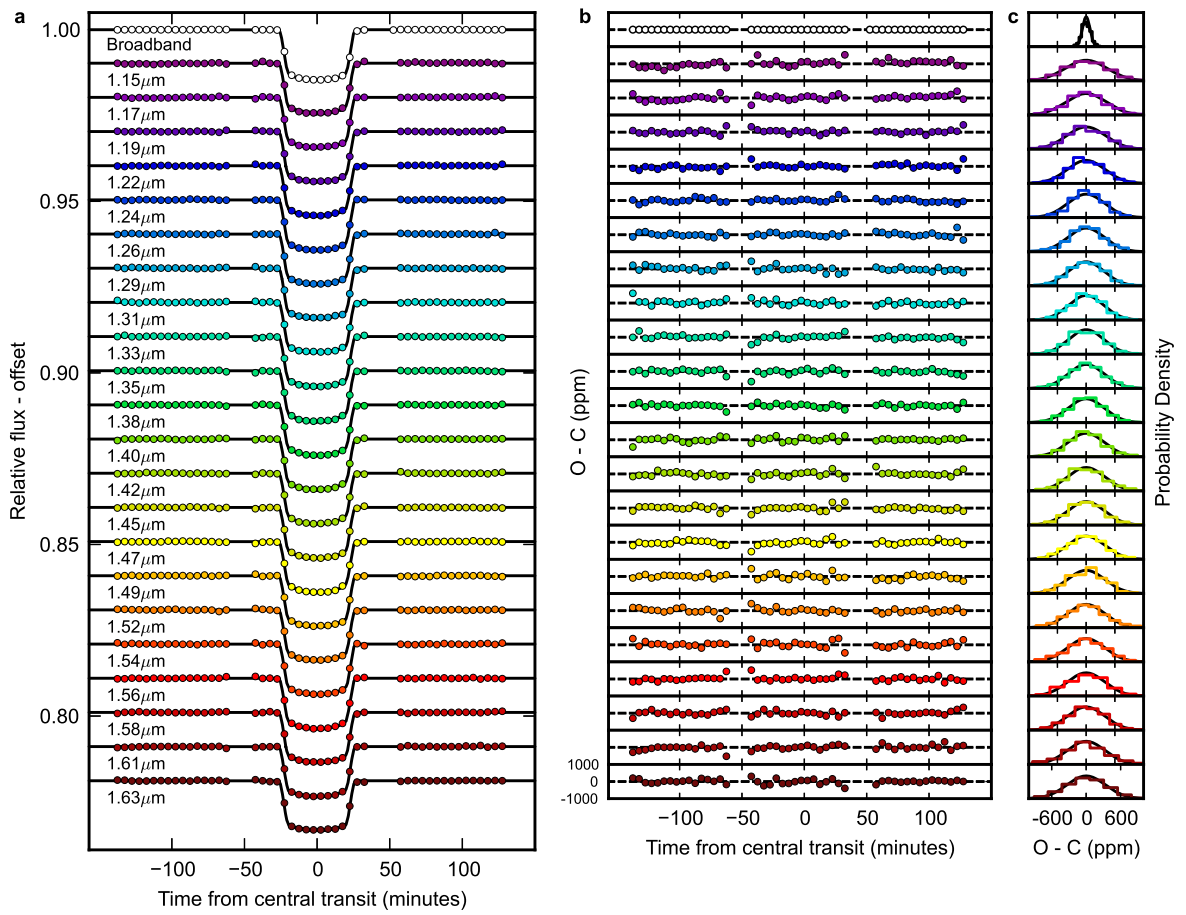
Author Contributions L.K. led the data analysis, with contributions from J.L.B., D.D., K.B.S., and A.S.; L.K., J.L.B, J.-M.D., and B.B. wrote the paper; J.L.B and J.-M.D. conceived the project and wrote the telescope time proposal with contributions from B.B., D.D., S.S., and Z.B.-T.; L.K., J.L.B., J.-M.D., D.D., and Z.B.-T. planned the observations; B.B. and S.S. developed and performed the theoretical modeling; D.H. calculated theoretical stellar limb darkening; J.L.B. led the overall direction of the project. All authors discussed the results and commented on the manuscript.

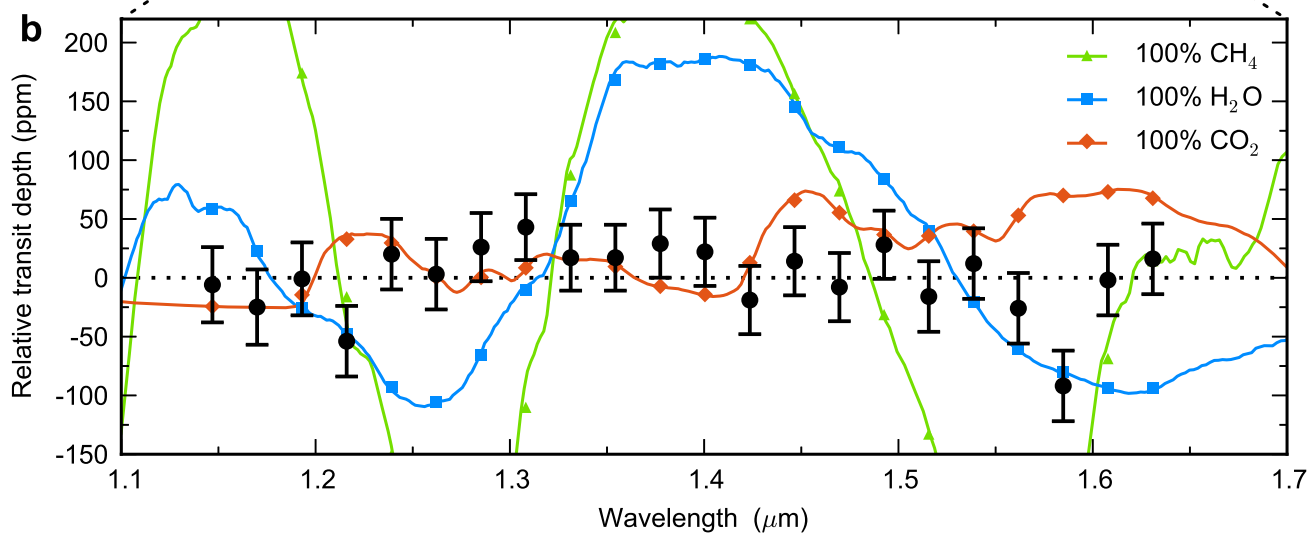
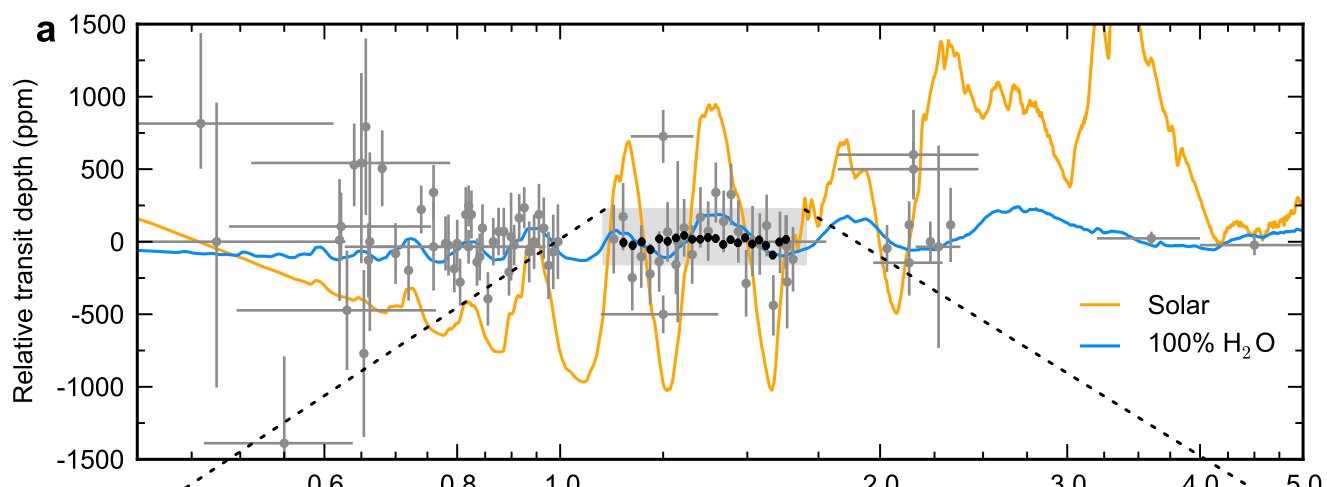
Author Information The data utilized in this work can be accessed at the NASA Mikulski Archive for Space Telescopes (<http://archive.stsci.edu>). Reprints and permissions information is available at www.nature.com/reprints. The authors declare that they have no competing financial interests. Correspondence and request for materials should be addressed to L.K. (laura.kreidberg@uchicago.edu).

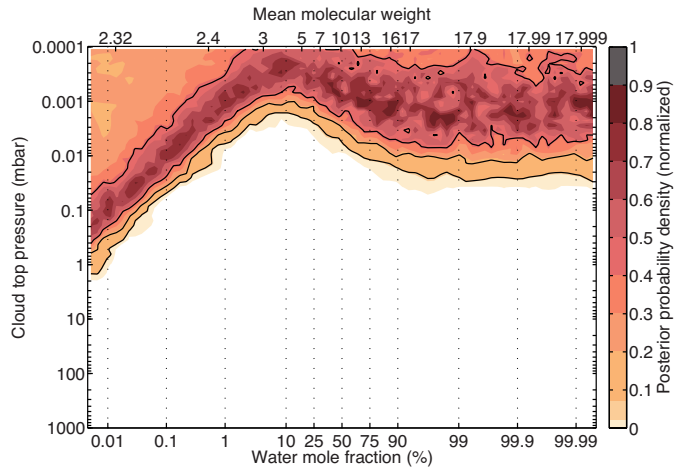
Figure 1 Spectrophotometric data for transit observations of GJ 1214b. **a**, Normalized and systematics-corrected data (points) with best-fit transit models (lines), offset for clarity. The data consist of 11 transit observations and are binned in phase in 5-minute increments. The spectroscopic light curve fit parameters are transit depth, a linear limb darkening coefficient, and a normalization term to correct for systematics. A unique transit depth is determined for each observation and the measured transit depths are consistent from epoch to epoch in all channels. **b**, Binned residuals from the best-fit model light curves. The residuals are within 14% of the predicted photon-limited shot noise in all spectroscopic channels. The median observed rms in the spectroscopic channels is 315 ppm, prior to binning. **c**, Histograms of the unbinned residuals (colored lines) compared to the expected photon noise (black lines). The residuals are Gaussian, satisfying a Shapiro-Wilk test for normality at the $\alpha = 0.1$ level in all but one channel ($1.24 \mu\text{m}$). The median reduced χ^2 value for the spectroscopic light curve fits is 1.02.

Figure 2 The transmission spectrum of GJ 1214b. **a**, Transmission spectrum measurements from our data (black points) and previous work (grey points)⁶⁻¹⁸, compared to theoretical models (lines). Each data set is plotted relative to its mean. Previous data rule out a cloud-free solar composition (orange line), but are consistent with a high-mean molecular weight atmosphere or a hydrogen-rich atmosphere with high-altitude clouds. **b**, Detail view of our measured transmission spectrum (black points) compared to high mean molecular weight models (lines). The error bars are 1σ uncertainties in the posterior distribution from a Markov chain Monte Carlo fit to the light curves (see the Supplemental Information for details of the fits). The colored points correspond to the models binned at the resolution of the observations. The data are consistent with a featureless spectrum ($\chi^2 = 22.3$ for 21 degrees of freedom), but inconsistent with cloud-free high-mean molecular weight scenarios. Fits to pure water, methane, carbon monoxide, and carbon dioxide models have $\chi^2 = 321.2, 963.3, 104.6,$ and 74.5 with 21 degrees of freedom, and are ruled out at $15.7, 29.4, 7.2,$ and 5.4σ confidence, respectively.

Figure 3 Spectral retrieval results for a two-component (hydrogen/helium and water) model atmosphere for GJ 1214b. The colors indicate posterior probability density as a function of water mole fraction and cloud top pressure. Black contours mark the 1, 2, and 3σ Bayesian credible regions. Clouds are modeled with a gray opacity, with transmission truncated below the cloud altitude. The atmospheric modeling assumes a surface gravity of 8.48 m/s^2 and an equilibrium temperature equal to 580 K. The data require clouds at a minimum pressure of 1 mbar (3σ confidence) to reproduce the observed featureless transmission spectrum, regardless of the atmospheric mean molecular weight.







Supplementary Information

The supplementary information describes the observations, data reduction, systematics correction, and light curve fitting for 13 transits of GJ 1214b.

Observations

We observed 13 transits of the super-Earth exoplanet GJ 1214b with the Wide Field Camera 3 (WFC3) instrument on the Hubble Space Telescope (HST) between UT 27 September 2012 and 4 August 2013. Each transit observation (or visit) consisted of four 96-minute HST orbits of time series spectroscopy, with 45-minute gaps in data collection in each orbit due to Earth occultation. We employed the G141 grism, which covers the wavelength range 1.1 to 1.7 μm . The spectra were binned at resolution $R \equiv \lambda/\Delta\lambda \sim 70$. To optimize the efficiency of the observations, we used spatial scan mode, which moves the spectrum perpendicular to the dispersion direction during the exposure. Spatial scanning enables longer exposures for bright targets that would otherwise saturate, such as GJ 1214. We used a 0.12"/second scan rate for all exposures, which yielded peak per pixel counts near 23,000 electrons (30% of saturation). An example raw data frame is shown in Figure S1.

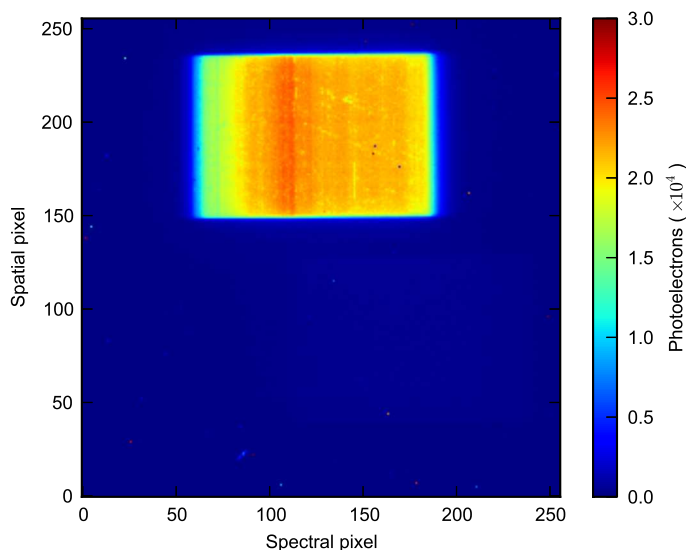


Figure S1: An example spatially scanned raw data frame. The exposure time was 88.4 s.

The observations had the following design. At the beginning of each orbit, we took a direct image with the F130N narrowband filter to establish a wavelength zero-point. For the remainder of each orbit, we took spatially scanned exposures with the G141 grism. Each observation used the 256×256 subarray. During the first five transit observations, we took 88.4 s exposures with the SPARS10, NSAMP=13 readout mode and scanned in the forward direction only. Each exposure contains NSAMP non-destructive reads. For transit observations 6 – 13, we modified our approach to reduce overhead time: we increased the exposure time to 103.1 s using the mode SPARS10, NSAMP=15, and scanned successively forward and backward. These approaches yielded 67 and 75 spectra per visit with duty cycles of 58% and 76%, respectively. One transit observation (UT 12 April 2013) was unsuccessful because the Fine Guidance Sensors failed to reacquire the guide stars. We do not use data from this observation in our analysis. We also exclude data from the transit observation on UT 4 August 2013, which showed evidence for a starspot crossing. Our final analysis therefore used 11 transit observations.

Data reduction

Our data reduction process begins with the “*ima*” data product from the WFC3 calibration pipeline, *calwf3*. These files are bias- and dark current-subtracted and flagged for bad pixels. For spatially scanned data, each pixel is illuminated by the stellar spectrum for only a small fraction of the exposure; the remainder of time it collects background. To aid in removing the background, we form subexposures of each image by subtracting consecutive non-destructive reads. A subexposure thus contains photoelectrons gathered during the 7.4 s between two reads. We reduce each subexposure independently, as follows. First we apply a wavelength-dependent flat field correction. Next we mask bad pixels that have been flagged data quality $DQ = 4, 32, \text{ or } 512$ by *calwf3*. To estimate the background collected during the subexposure, we draw conservative masks around all stellar spectra, measure the background from the median of the unmasked pixels, and subtract it. We compute a variance for the spectrum accounting for photon shot noise, detector read noise, and uncertainty in the background estimation.

We next correct for the wavelength dependence of the spectrum on detector position. The grism dispersion varies along the spatial direction of the detector, so we calculate the dispersion

solution for each row in the subexposure and interpolate to the wavelength scale corresponding to the direct image position. This interpolation also corrects bad pixels. We then create a 40-pixel tall extraction box centered on the middle of the spatial scan and extract the spectrum with an optimal extraction routine³¹. Because each row has been interpolated to a common wavelength scale, the final spectrum is constructed by summing the spectra from all the subexposures. See Figure S2 for an example spectrum.

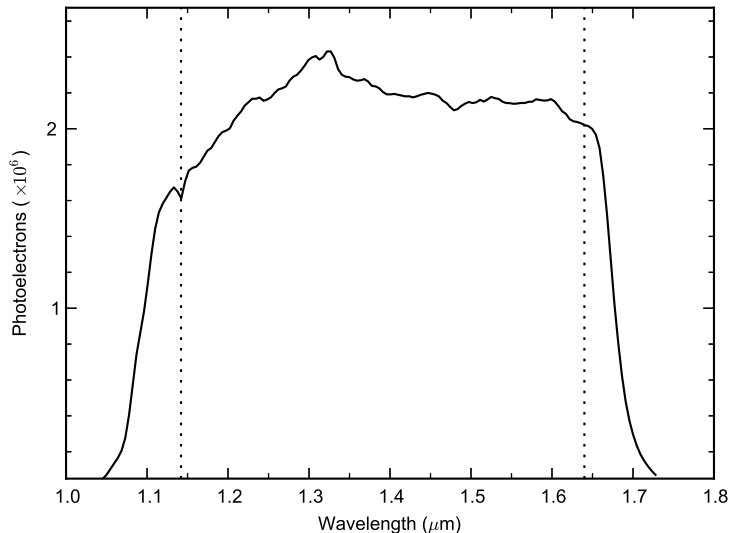


Figure S2: An example extracted spectrum for an 88.4 s exposure. The dotted lines indicate the wavelength range over which we measure the transmission spectrum.

Finally, we account for dispersion-direction drift of the spectra during each visit and between visits. Using the first exposure of the first visit as a template, we determine a shift in wavelength-space that minimizes the difference between each subsequent spectrum and the template. The best fit shift values are less than 0.1 pixel, both within each visit and between visits. We interpolate each spectrum to an average wavelength scale, offset from the template by the mean of the estimated wavelength shifts. This step does not have a significant effect on our results. We bin the spectra in 5-pixel-wide channels, obtaining 29 spectroscopic light curves covering the wavelength range 1.05 – 1.70 μm . The data near the edges of the grism response curve exhibit more pronounced systematics, so we restrict our analysis to 22 spectroscopic

channels between 1.15 and 1.63 μm . The limits are shown in Figure S2.

Systematics correction

The light curves exhibit a ramp-like systematic similar to those seen in other WFC3 transit spectroscopy data^{12,25}. The ramp has a larger amplitude and a different shape in the first orbit compared to subsequent orbits, so we exclude data from the first orbit in our light curve fits, following standard practice. We correct for systematics in orbits 2 – 4 using two methods:

Method 1: `model-ramp`

This method fits an analytic function to the systematics¹². The function has the form:

$$S = S_0(C + Vt_v)(1 - R_{\text{orb}}e^{-t_{\text{orb}}/\tau}) \quad (1)$$

where S is the observed light curve, S_0 is the model for the intrinsic, systematics-free transit light curve, t_v is the time elapsed since the first exposure in a visit, t_{orb} is the time elapsed since the first exposure in an orbit, C is a normalization, V is a visit-long slope, R_{orb} is a ramp amplitude, and τ is a ramp timescale. The parameters C , V , and τ are constrained to be constant for each visit, but R_{orb} is permitted to vary between orbits.

Method 2: `divide-white`

The second method assumes the systematics are wavelength-independent and can be modeled with a scaled vector of white light curve systematics^{24,26}. Quantitatively, the white light curve is modeled by

$$W = Z \cdot W_0 \quad (2)$$

where W is the observed white light curve, W_0 is the intrinsic white light curve, and Z is a vector of systematics. We represent W_0 using the best-fit model from the model-ramp technique and solve for Z . An example white light curve and best fit intrinsic white light curve are shown in Figure S3.

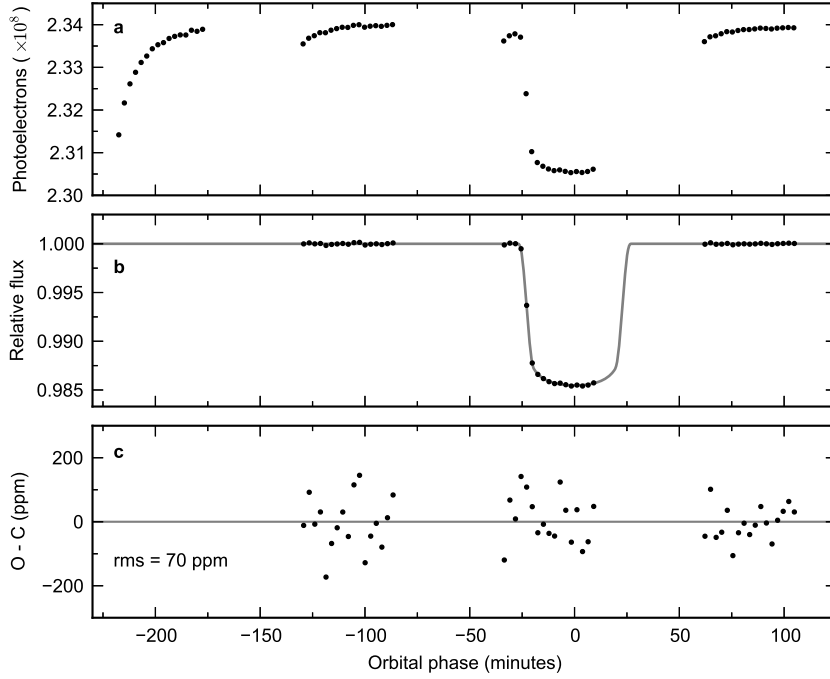


Figure S3: **a**, The broadband light curve from the first transit observation. **b**, The broadband light curve corrected for systematics using the `model-ramp` technique (points) and the best-fit model (line). **c**, Residuals from the white light curve fit.

The spectroscopic light curves S are modeled as

$$S = C \cdot Z \cdot S_0 \quad (3)$$

where C is a normalization constant specific to each spectral channel. We observe that the systematics have similar amplitude and form across the wavelength range of our observations, hence the viability of the `divide-white` technique. The WFC3 systematics depend on the peak per pixel fluence²⁵, but as can be seen in Figure 2, the product of the stellar spectrum and the G141 grism response is nearly uniform over the 1.1 – 1.7 μm range.

Light curve fits

We fit the spectroscopic light-curves with both the `divide-white` and `model-ramp` methods and determined the best-fit parameters and errors with a Markov chain Monte Carlo (MCMC) algorithm. We divided the light curves into 17 data sets (11 visits, with 2 data sets for 6 of the visits), separated by transit epoch and spatial scan direction, to account for a normalization offset between the forward-scanned and reverse-scanned light curves. Each light curve was fit with five 10^5 step MCMC chains, with 2.5×10^4 burn-in steps removed from each chain. We tested for convergence using the Gelman-Rubin diagnostic. The results reported are from the five chains combined. We held the orbital parameters fixed at the best-fit values for the white light curve: inclination $i = 89.1^\circ$, the ratio of the semi-major axis to the stellar radius $a/R_s = 15.25$, the orbital period $P = 1.58040464894$ days, and the time of central transit $T_c = 2454966.52507$ BJD_{TDB}. We assume a circular orbit. The free parameters for the `divide-white` fit are a linear limb darkening parameter u , a normalization constant C , and the planet-to-star radius ratio R_p/R_s . The `model-ramp` fit had an additional visit-long slope parameter V , ramp amplitudes R_{orb} , and a ramp timescale τ . The ramp amplitudes for orbits 3 and 4 were constrained to be equal within each data set. For both methods, we fit for transit depth at each epoch, one limb darkening parameter for all epochs, and unique systematic parameters for each data set, yielding a total of 29 and 97 free parameters per channel for the `divide-white` and `model-ramp` fits, respectively. Each spectral channel was analyzed independently. The priors for each free parameter were uniform. We show the posterior distributions of the parameters in Figure S4, and note that they have little correlation with the transit depth. The measured transit depths are consistent from epoch to epoch, as shown in Figure S5. The `divide-white` and `model-ramp` techniques yield consistent results. We report the transit depths and limb darkening coefficients from the `divide-white` method in Table S1. The transit depths given are the weighted averages over all epochs, minus the mean transit depth over all channels (0.013413).

The derived limb darkening coefficients are shown in Figure S6. These results illustrate the importance of careful treatment of limb darkening for cool stars. There is a peak in the

Table 1: Derived parameters for the light curve fits

Wavelength (μm)	Relative Transit Depth (ppm)	Limb Darkening	χ^2_ν (568 dof)
1.137 – 1.161	-6 ± 32	0.27 ± 0.01	1.12
1.161 – 1.184	-25 ± 32	0.27 ± 0.01	1.02
1.184 – 1.207	-1 ± 31	0.27 ± 0.01	1.05
1.207 – 1.223	-54 ± 30	0.27 ± 0.01	0.91
1.223 – 1.252	20 ± 30	0.28 ± 0.01	0.86
1.252 – 1.276	3 ± 30	0.26 ± 0.01	0.96
1.276 – 1.299	26 ± 29	0.23 ± 0.01	1.01
1.299 – 1.322	43 ± 28	0.24 ± 0.01	0.96
1.322 – 1.345	17 ± 28	0.27 ± 0.01	1.06
1.345 – 1.368	17 ± 28	0.31 ± 0.01	0.99
1.369 – 1.391	29 ± 29	0.29 ± 0.01	0.93
1.391 – 1.414	22 ± 29	0.30 ± 0.01	0.98
1.414 – 1.437	-19 ± 29	0.31 ± 0.01	1.13
1.437 – 1.460	14 ± 29	0.30 ± 0.01	1.02
1.460 – 1.483	-8 ± 29	0.32 ± 0.01	1.02
1.483 – 1.506	28 ± 29	0.29 ± 0.01	0.97
1.506 – 1.529	-16 ± 30	0.28 ± 0.01	1.18
1.529 – 1.552	12 ± 30	0.28 ± 0.01	1.19
1.552 – 1.575	-26 ± 30	0.29 ± 0.01	1.17
1.575 – 1.598	-91 ± 30	0.27 ± 0.01	1.03
1.598 – 1.621	1 ± 30	0.26 ± 0.01	1.40
1.621 – 1.644	16 ± 30	0.23 ± 0.01	1.14

coefficients near $1.45 \mu\text{m}$ that is due to the presence of water in the star. We find that fixing the limb darkening coefficients to a constant value in all spectral channels introduces a spurious water feature in the transmission spectrum.

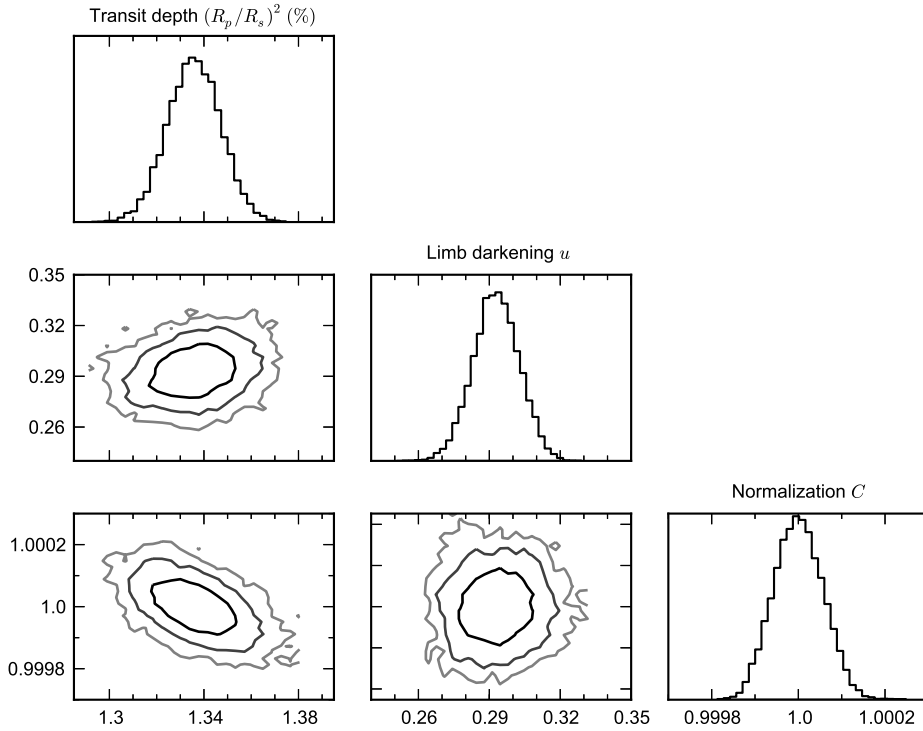


Figure S4: The posterior distributions for the `divide-white` fit parameters for the $1.40\ \mu\text{m}$ channel from the first transit observation. The diagonal panels show histograms of the Markov chains for each parameter. The off-diagonal panels show contour plots for pairs of parameters, with lines indicating the 1, 2, and 3σ confidence intervals for the distribution. The normalization constant is divided by its mean.

References

- [31] Horne, K. An optimal extraction algorithm for CCD spectroscopy. *Pub. Astron. Soc. Pacific* **98**, 609–617 (1986).
- [32] Anglada-Escudé, G., Rojas-Ayala, B., Boss, A. P., Weinberger, A. J. & Lloyd, J. P. GJ 1214 reviewed. Trigonometric parallax, stellar parameters, new orbital solution, and bulk properties for the super-Earth GJ 1214b. *Astron. Astrophys.* **551**, A48 (2013).

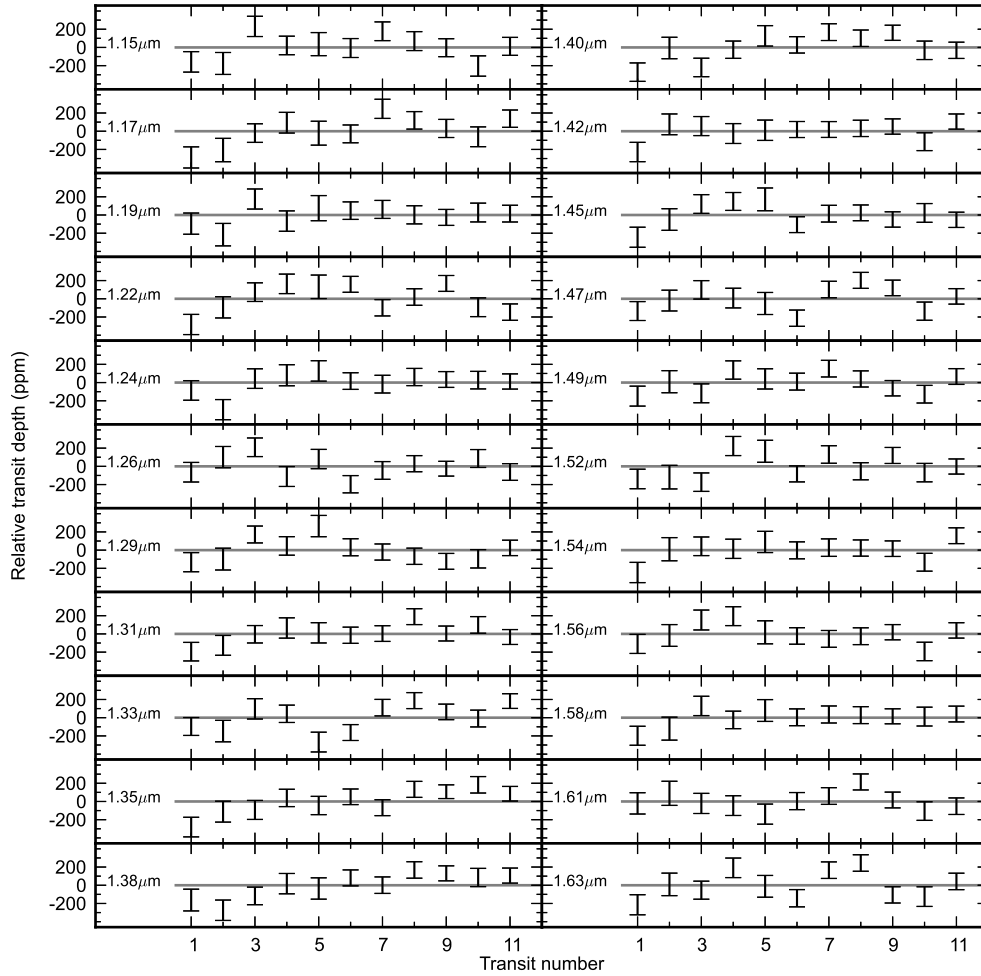


Figure S5: Transit depths relative to the mean in 22 spectroscopic channels, for the 11 transits analyzed. The black error bars indicate the 1σ uncertainties determined by MCMC.

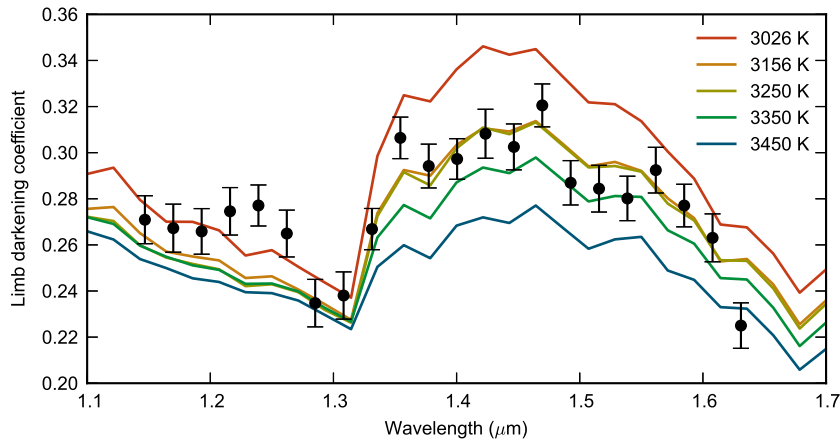


Figure S6: Fitted limb darkening coefficients as a function of wavelength (black points) and theoretical predictions for stellar atmospheres with a range of temperatures (lines). The uncertainties are 1σ confidence intervals from an MCMC. The temperature of GJ 1214 is estimated to be 3250 K³².